Test Problems for Potential Field Source Surface Extrapolations of Solar and Stellar Magnetic Fields

DAVID STANSBY[1] AND DANIEL VERSCHAREN[1]

[1]*Mullard Space Science Laboratory, University College London, Holmbury St. Mary, Surrey RH5 6NT, UK*

ABSTRACT

The potential field source surface (PFSS) equations are commonly used to model the coronal magnetic field of the Sun and other stars. As with any computational model, solving equations using a numerical scheme introduces errors due to discretisation. We present a set of tests for quantifying these errors by taking advantage of analytic solutions to the PFSS equations when the input field is proportional to a single spherical harmonic. From the spherical harmonic solutions we derive analytic equations for magnetic field lines traced through the three dimensional magnetic field solution. We propose these as a set of standard analytic solutions that all PFSS solvers should be tested against to quantify their inherent errors. We apply these tests to the `pfsspy` software package, showing that it reproduces spherical harmonic solutions well with a slight overestimation of the unsigned open magnetic flux. It is also successful at reproducing analytic field line equations, with errors in field line footpoints typically much less than one degree.

1. INTRODUCTION

The potential field source surface (PFSS) set of equations (Altschuler & Newkirk 1969; Schatten et al. 1969) are commonly used to model the coronal magnetic field of the Sun (e.g. Badman et al. 2020; Stansby et al. 2021; Fargette et al. 2021) and other stars (e.g. Jardine et al. 2017; Saikia et al. 2020; Kochukhov 2020). The key assumption of PFSS models is the absence of electric current within the domain of interest. Under this assumption the electromagnetic equations for the magnetic field (**B**) reduce to

$$\nabla \cdot \mathbf{B} = 0 \tag{1}$$
$$\nabla \times \mathbf{B} = \mathbf{0} \tag{2}$$

These equations are equivalent to the Laplace equation,

$$\nabla^2 \Phi = 0, \tag{3}$$

where the scalar potential is defined as $\mathbf{B} = \nabla \Phi$. The solution is derived between the stellar surface (at a radius $r_\odot$) and a specified source surface (at a radius $r_{ss} > r_\odot$), and three boundary conditions are required for a unique solution. One of these is given by a single component of the magnetic field at the inner boundary ($r = r_\odot$), and the other two are set by the assumption that the field is purely radial (ie. the two transverse components are zero) on the outer boundary ($r = r_{ss}$). The second assumption is motivated by accelerating stellar wind plasma forcing the field to be near-radial at the source surface.

Different numerical methods are available for solving the above equations, including spherical harmonic expansions (e.g. Altschuler & Newkirk 1969; Hakamada 1995; Tóth et al. 2011) and finite difference methods (e.g. Jiang & Feng 2012; Tóth et al. 2011; Caplan et al. 2021). To understand the topology of the magnetic field (e.g. van Driel-Gesztelyi et al. 2012; Boe et al. 2020; Baker et al. 2021) and how stellar wind flows through a corona (e.g. Neugebauer et al. 1998; Stansby et al. 2020a), magnetic field line connectivities between the outer and inner boundaries are also needed, which requires tracing magnetic field lines through the three-dimensional magnetic field solution using a field line tracer.

In order to check whether numerical methods work as expected, and to quantify any errors inherent in the numerical scheme employed, it is helpful to compare their output with exact analytical solutions. While in some areas such as hydrodynamic modelling test problems are common (Sod 1978), to our knowledge no such test problems have been published for PFSS solvers and field line tracers.

In this paper we provide a set of analytical solutions for the PFSS equations (Section 2.1) and use these to derive solutions for the unsigned open flux at the source surface (Section 2.2) and field lines traced through these solutions (Section 2.3). We then compare these to the numerical solutions computed by the `pfsspy` solver (Stansby et al. 2020b) (Section 4), to demonstrate its usefulness, accuracy, and limitations.

2. ANALYTICAL SOLUTIONS

In this section we recount analytical solutions to the PFSS equations using spherical harmonics (Section 2.1). Using these solutions we then derive equations for the total open magnetic flux (Section 2.2) and magnetic field lines traced through the spherical harmonic solutions (Section 2.3).

2.1. *PFSS solutions*

Following Wang & Sheeley (1992); Mackay & Yeates (2012), when the radial component of the magnetic field on the stellar surface ($r_\odot$) is specified the general solution to the PFSS equations in a spherical coordinate system is given by the spherical harmonic decomposition

$$B_r = \sum_{\ell=1}^{\infty} \sum_{m=-\ell}^{m=\ell} a_{\ell m} c_\ell(r) Y_{\ell m}(\theta, \phi) \tag{4}$$

$$B_\theta = \sum_{l=1}^{\infty} \sum_{m=-\ell}^{m=\ell} a_{\ell m} d_\ell(r) \frac{\partial Y_{\ell m}(\theta, \phi)}{\partial \theta} \tag{5}$$

$$B_\phi = \sum_{\ell=1}^{\infty} \sum_{m=-\ell}^{m=\ell} a_{\ell m} d_\ell(r) \frac{1}{\sin\theta} \frac{\partial Y_{\ell m}(\theta, \phi)}{\partial \phi} \tag{6}$$

where

$$Y_{\ell m}(\theta, \phi) = A_{\ell m} P_{\ell m}(\cos\theta) \begin{cases} \cos m\phi \\ \sin m\phi \end{cases} \quad \begin{matrix} m > 0 \\ m \le 0 \end{matrix} \tag{7}$$

are real spherical harmonics, $A_{\ell m}$ are normalisation coefficients and $P_{\ell m}$ are the associated Legendre polynomials.

$a_{\ell m}$ are constant coefficients derived from the input magnetic field via.

$$a_{\ell m} = \int_0^{2\pi} d\phi \int_0^{\pi} \sin\theta d\theta \; B_{r\odot}(\theta, \phi) Y_{\ell m}(\theta, \phi) \tag{8}$$

and the functions c_ℓ and d_ℓ are

$$c_\ell(z) = \left(\frac{r}{r_\odot}\right)^{-\ell-2} \left[\frac{\ell+1 + \ell(r/r_{ss})^{2\ell+1}}{\ell+1 + \ell(r_\odot/r_{ss})^{2\ell+1}}\right] \tag{9}$$

$$d_\ell(z) = \left(\frac{r}{r_\odot}\right)^{-\ell-2} \left[\frac{1 - (r/r_{ss})^{2\ell+1}}{\ell+1 + \ell(r_\odot/r_{ss})^{2\ell+1}}\right] \tag{10}$$

The polar coordinate range is $[0, \pi]$, with $\theta = 0$ the north pole.

If the input magnetic field is directly proportional to a single spherical harmonic, $B_r = B_0 Y_{\ell'm'}$ where B_0 is a constant, and the $a_{\ell m}$ coefficients simplify greatly to

$$a_{\ell m} = B_0 \delta_{\ell\ell'} \delta_{mm'} \tag{11}$$

and only a single term in each sum is non-zero. For the remainder of this paper we set the input magnetic field proportional to a single spherical harmonic, so for brevity drop the apostrophes that denote a specific choice of ℓ, m. Under these assumptions the solutions are

$$B_r = B_0 c_\ell(r) Y_{\ell m}(\theta, \phi) \tag{12}$$

$$B_\theta = B_0 d_\ell(r) \frac{\partial Y_{\ell m}(\theta, \phi)}{\partial \theta} \tag{13}$$

$$B_\phi = B_0 d_\ell(r) \frac{1}{\sin\theta} \frac{\partial Y_{\ell m}(\theta, \phi)}{\partial \phi} \tag{14}$$

In the next sections we provide equations for calculating the total unsigned open flux (Section 2.2) and magnetic field line equations (Section 2.3) from these solutions.

2.2. *Open flux*

The total unsigned open flux is defined by integrating the radial component of the magnetic field on the source surface

$$\Phi_{open} = r_{ss}^2 \int_0^{2\pi} \int_0^{\pi} |B_r(\theta, \phi, r_{ss})| \sin\theta d\theta d\phi \tag{15}$$

For a single harmonic this simplifies to

$$\Phi_{open} = r_{ss}^2 B_0 c_\ell(r_{ss}) \int_0^{2\pi} \int_0^{\pi} |Y_{\ell m}(\theta, \phi)| \sin\theta d\theta d\phi \tag{16}$$

We numerically evaluated the double integral to get a number for the analytic open flux when comparing to values computed from the PFSS solver.

2.3. *Magnetic field lines*

In spherical coordinates the magnetic field tracing equations are

$$\frac{dr}{ds} = \hat{B}_r \tag{17}$$

$$\frac{d\theta}{ds} = \frac{\hat{B}_\theta}{r} \tag{18}$$

$$\frac{d\phi}{ds} = \frac{\hat{B}_\phi}{r\sin\theta} \tag{19}$$

where the paramater s is the physical distance along the field line, and $\hat{B}_i := B_i/|\mathbf{B}|$ are components of a unit vector pointing in the direction of the magnetic field. These form a set of three coupled equations that can be integrated from an initial seed point to evaluate coordinates along a magnetic field line.

In the case where the input field is proportional to a single spherical harmonic, equations 12 – 14 can be

substituted in and ds eliminated to give

$$\frac{d\theta}{dr} = \left[\frac{1}{r}\frac{d_\ell(r)}{c_\ell(r)}\right]\left[\frac{1}{Y_{\ell m}}\frac{\partial Y_{\ell m}(\theta,\phi)}{\partial\theta}\right] \tag{20}$$

$$\frac{d\phi}{dr} = \frac{1}{r\sin^2\theta}\frac{d_\ell(r)}{c_\ell(r)}\left[\frac{1}{Y_{\ell m}}\frac{\partial Y_{\ell m}(\theta,\phi)}{\partial\phi}\right] \tag{21}$$

$$\frac{d\theta}{d\phi} = \sin^2\theta\left[\frac{\partial Y_{\ell m}(\theta,\phi)}{\partial\theta}\right]\left[\frac{\partial Y_{\ell m}(\theta,\phi)}{\partial\phi}\right]^{-1} \tag{22}$$

Because the spherical harmonics are separable in θ,ϕ, equation 20 is a function of only r and θ and equation 22 is only a function of ϕ and θ. This decouples the three field line tracing equations, allowing two of them to be integrated independently to give the longitude and latitude as functions of radius. In the following subsections we integrate these two equations and give analytic solutions for field lines in a spherical harmonic solution.

2.3.1. *The θ field line equation*

To find $\theta(r)$ we start by separating variables and integrating Equation 20

$$\int_{\theta_{ss}}^{\theta} P_{\ell m}(\bar{\theta})\left[\frac{\partial P_{\ell m}(\bar{\theta})}{\partial\bar{\theta}}\right]^{-1} d\bar{\theta} = \int_{r_{ss}}^{r}\frac{1}{\bar{r}}\frac{d_\ell(\bar{r})}{c_\ell(\bar{r})}d\bar{r} \tag{23}$$

Barred symbols denote dummy integration variables. To trace field lines down from the source surface to the solar surface, the radial integration limits are set to the source surface radius, r_{ss} and the radial coordinate along the field line, r. The θ integration limits set to a fixed initial latitude θ_{ss}, and the latitude along the field line, θ. Defining $\rho = r/r_{ss}$, the radial integration is given in equation 23 of Gregory (2011) as

$$\int_{r_{ss}}^{r}\frac{1}{\bar{r}}\frac{d_\ell(\bar{r})}{c_\ell(\bar{r})}d\bar{r} = \frac{1}{\ell}\frac{1}{\ell+1}\ln\left[\frac{\rho^\ell(2\ell+1)}{l\rho^{2\ell+1}+(\ell+1)}\right] \tag{24}$$

The θ integration on the left hand side of equation 23 is more complicated – Gregory (2011) give a general solution for the left hand side of 23 $\forall\ell$ and $m = 0$, but for $\ell > 1$ the solution is not available in closed form. Instead we rearrange the integral on the left hand side of equation 23 to define the function

$$f_{\ell m}(\theta) := \exp\left[2l\int_{\theta_{ss}}^{\theta} P_{\ell m}(\bar{\theta})\left[\frac{\partial P_{\ell m}(\bar{\theta})}{\partial\bar{\theta}}\right]^{-1} d\bar{\theta}\right] \tag{25}$$

With this definition, equations 24 and 25 are substituted into equation 23 to give the equation for $\theta(r)$ along a field line

$$f_{\ell m}(\theta) = f_{\ell m}(\theta_{ss})\left[\frac{\rho^\ell(2\ell+1)}{\ell\rho^{2\ell+1}+(\ell+1)}\right]^{\frac{2}{\ell+1}} \tag{26}$$

Table 1. Low order associated Legendre polynomials, and related functions. See Equation 25 for the definition of $f_{\ell m}$ and Equation 29 for the definition of $g_{\ell m}$. The functions listed are the same for $m \to -m$.

l, m	$P_{\ell m}$	$f_{\ell m}(\theta)$	$g_{\ell m}(\theta)$
1, 0	$\cos\theta$	$\sin^2\theta$	
1, 1	$\sin\theta$	$\cos^2\theta$	$\frac{\sin\theta}{\cos\theta}$
2, 0	$3\cos^2\theta - 1$		
2, 1	$\cos\theta\sin\theta$	$\cos 2\theta$	$\frac{\sin\theta}{\sqrt{\cos 2\theta}}$
2, 2	$\sin^2\theta$	$\cos^2\theta$	$\left(\frac{\sin\theta}{\cos\theta}\right)^2$
3, 0	$5\cos^3\theta - 3\cos\theta$		
3, 1	$(5\cos^2\theta - 1)\sin\theta$		
3, 2	$\cos\theta\sin^2\theta$	$3\cos(2\theta) + 1$	$\frac{\sin^2\theta}{2-3\sin^2\theta}$
3, 3	$\sin^3\theta$	$\cos^2\theta$	$\frac{\sin\theta}{\cos\theta}$

The functions $f_{\ell m}(\theta)$ for low order spherical harmonics are tabulated in Table 1. Solving this equation analytically requires that the inverse of $f_{\ell m}$ exist in a closed form.

2.3.2. *The ϕ field line equation*

Equation 22 is the field line equation relating θ and ϕ. For $m = 0$, $B_\phi = 0$ and this has the trivial solution $\phi = const$, so we only consider the $m \neq 0$ case.

Separating variables and integrating gives

$$\int_{\theta_{ss}}^{\theta}\frac{P_{\ell m}}{\sin\bar{\theta}^2}\left[\frac{\partial P_{\ell m}}{\partial\bar{\theta}}\right]^{-1} d\bar{\theta} = \int_{\phi_{ss}}^{\phi} Y_{\ell m}\left[\frac{\partial Y_{\ell m}}{\partial\bar{\phi}}\right]^{-1} d\bar{\phi} \tag{27}$$

The ϕ integration on the right hand side evaluates as

$$\int_{\phi_{ss}}^{\phi} Y_{\ell m}\left[\frac{\partial Y_{\ell m}}{\partial\bar{\phi}}\right]^{-1} d\bar{\phi} = \frac{1}{m^2}\begin{cases}\ln\frac{\sin m\phi_{ss}}{\sin m\phi} & m > 0 \\ \ln\frac{\cos m\phi_{ss}}{\cos m\phi} & m < 0\end{cases} \tag{28}$$

For low order spherical harmonics the integral on the left hand side of 27 is rearranged to define the function

$$g_{\ell m}(\theta) := \exp\left[m^2\int_{\theta_{ss}}^{\theta}\frac{P_{\ell m}}{\sin\bar{\theta}^2}\left[\frac{\partial P_{\ell m}}{\partial\bar{\theta}}\right]^{-1} d\bar{\theta}\right] \tag{29}$$

The functions $g_{\ell m}$ for low order spherical harmonics are given in Table 1. Substituting equations 28 and 29 into 27 gives the the equation for ϕ as a function of r along a field line

$$\begin{cases}\frac{\sin m\phi}{\sin m\phi_{ss}} \\ \frac{\cos m\phi}{\cos m\phi_{ss}}\end{cases} = \frac{g_{\ell m}(\theta)}{g_{\ell m}(\theta_{ss})}\qquad\begin{matrix}m > 0 \\ m < 0\end{matrix} \tag{30}$$

Once $\theta(r)$ is known from solving equation 26, it is used in Equation 30 to solve for $\phi(\theta(r))$. Unlike $f_{\ell m}$, the

inverse of $g_{\ell m}$ does not need to exist in closed form to derive ϕ along a field line.

3. THE `pfsspy` SOLVER

We briefly recount how `pfsspy` calculates the PFSS solution, in order to understand the user configurable options that affect the accuracy of the solver. Details on the numerical scheme are available in the numerical methods document archived alongside the software (Stansby et al. 2022).

`pfsspy` uses a finite difference method (van Balle-gooijen et al. 2000, Appendix B) to calculate the magnetic vector potential on a grid regularly spaced in $z = \log(r/r_\odot)$, $\lambda = \cos\theta$, ϕ. The number of grid points in the angular dimensions, n_ϕ and n_θ, are fixed by the resolution of the input $B_{r\odot}$ grid which must span the full sphere. Since the smallest magnetograms widely used from the Sun have a grid size of of 360×180 in (longitude, latitude), for simplicity we keep this as the fixed angular grid size throughout the tests. The number of radial grid points, n_r is user configurable.

To trace magnetic field lines `pfsspy` offers two different field line tracers. Here we perform comparisons with the FORTRAN implementation[1], which is the fastest of the two.

The field line equations in the coordinates that `pfsspy` uses are

$$\frac{d\rho}{ds} = \hat{B}_\rho \tag{31}$$

$$\frac{d\lambda}{ds} = \sqrt{1-\lambda^2}\hat{B}_\lambda \tag{32}$$

$$\frac{d\phi}{ds} = \frac{1}{\sqrt{1-\lambda^2}}\hat{B}_\phi \tag{33}$$

In the field line tracer three equations are integrated numerically using a 4th order Runge-Kutta method with a fixed discrete step size, Δs, which is specified by the user as a fraction of the grid cell size in the radial direction, $\Delta r = \log(r_{ss}/r_\odot)/n_r$. Because the step size Δs is kept constant relative to the log-scaled grid, larger physical steps are taken further away from the solar surface at larger values of r.

4. ANALYTIC SOLUTIONS AS TEST PROBLEMS

In this section we compare the magnetic field on the source surface (Section 4.1), the open flux (Section 4.2), and the field line connectivity (Section 4.3) between analytic and numerical `pfsspy` solutions. For clarity analysis is limited to harmonics with $\ell \leq 5$. For the Sun

Table 2. Configurable parameters in the `pfsspy` solver and their values for each figure.

	n_ϕ, n_θ	n_r	Δs
Figure 1	(360, 180)	40	1
Figure 2	(360, 180)	Varied	1
Figure 3	(360, 180)	40	1
Figure 4	(360, 180)	40	Varied

these are the dominant harmonics at all times in the solar cycle (DeRosa et al. 2012).

A range of software is used for creating comparisons, including pfsspy (Stansby et al. 2020b), numpy (Harris et al. 2020), scipy (Virtanen et al. 2020), pandas (Reback et al. 2021), sympy (Meurer et al. 2017) and astropy (The Astropy Collaboration et al. 2018). Code for producing the comparisons is available in version 1.1.0 of the `pfsspy` repository[2] and is archived at Stansby et al. (2022).

In the numerical solutions we set default the grid sizes to $n_\phi = 360$, $n_\theta = 180$, $n_r = 40$, and the default field line tracing step size to $\Delta s = 1$. The following subsections show a series of different tests, where one of these parameters may be varied. In all tests the source surface height is set to $r_{ss} = 2r_\odot$. Each test has one or more corresponding figures. For a summary of which parameters are fixed or varied for each figure, see Table 2.

4.1. **B** *on the source surface*

The two transverse magnetic field components, $B_{\phi,\theta}$ must always be zero on the source surface within a PFSS solution. This is always the case in in `pfsspy` which forces $B_{\phi,\theta} = 0$ at $r = r_{ss}$.

To compare B_r at $r = r_{ss}$, equation 14 is evaluated at the same points as the numerical `pfsspy` solution. 1D cuts of both the analytic and `pfsspy` solutions at a constant longitude of $\phi = 15°$ are compared in Figure 1. `pfsspy` reproduces the analytic solutions well, with the magnitude of solutions slightly larger than the analytic solutions. This suggests that `pfsspy` systematically over-estimates the total unsigned open flux, which we investigate quantitively in the next section.

4.2. *Open flux*

---

[1] https://github.com/dstansby/streamtracer
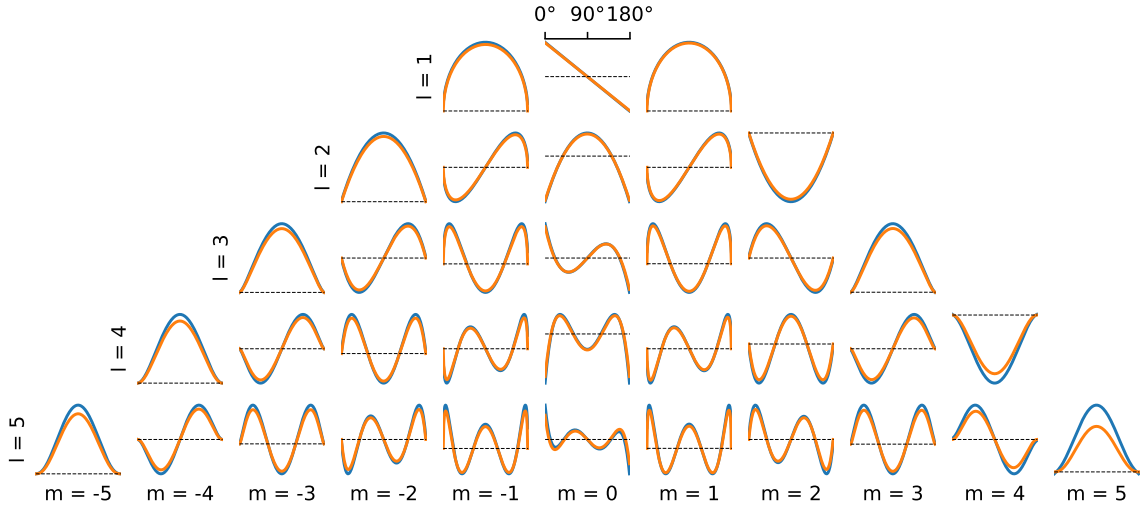
[2] https://github.com/dstansby/pfsspy

Figure 1. Comparison between analytic (orange) and `pfsspy` (blue) spherical harmonic solutions to the PFSS equations as functions of latitude at $r = r_{ss}, \phi = 15°$. Each panel represents a different spherical harmonic number, and plotted is the radial component of magnetic field. Dashed horizontal lines show $B_r = 0$.
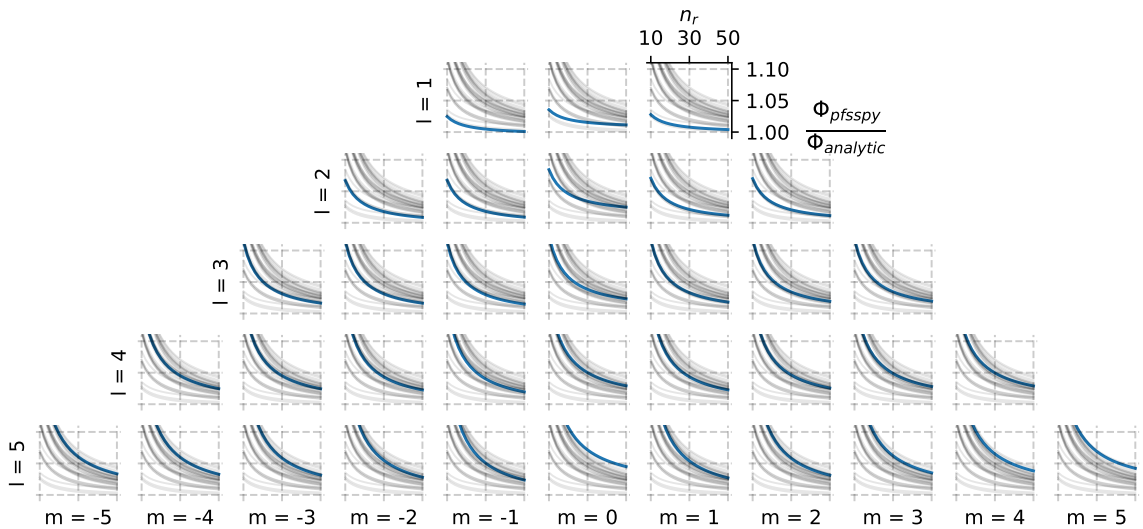

Figure 2. Ratio of unsigned open flux in numerical `pfsspy` solutions to analytic solutions as a function of number of radial cells within the `pfsspy` solution for various spherical harmonics.

Equation 16 gives an analytic integral for the unsigned open magnetic flux, which we evaluate using the `nquad` integration function in `scipy`. To check the accuracy of the integration we successfully verify the result against the analytical solution to the integral for $\ell, m = 1, 0$:

$$\Phi_{open}/B_0 = c_1 \left(r_{ss} \right) \int_0^{2\pi} d\phi \int_0^{\pi} |\cos \theta| \sin \theta d\theta \qquad (34)$$

$$= \frac{3}{2z_{ss}^3 + 1} \cdot 2\pi \cdot 2 \int_0^{\pi/2} \cos \theta \sin \theta d\theta \qquad (35)$$

$$= \frac{6\pi}{2z_{ss}^3 + 1} \qquad (36)$$

To evaluate the total unsigned open flux within a `pfsspy` result the magnetic field values on the source surface is multiplied by the area of their associated cell and summed over the full sphere.

Figure 2 shows the ratio of open flux in `pfsspy` results to the analytic value as a function of the number of radial grid points for spherical harmonics up to $\ell = 5$. As hinted from Figure 1, the unsigned open fluxes within `pfsspy` are systematically larger than the analytic solution. This difference decreases with an increasing number of radial grid cells, approaching asymptotic values of $\leq 5\%$ at around $n_r = 40$. This motivates our choice of $n_r = 40$ for the default number of radial grid cells –

with more radial cells there is not a significant reduction in the open flux error.

At larger values of ℓ the error in unsigned open flux increases from $\sim 1\%$ at $\ell = 1$ to $\sim 5\%$ at $\ell = 5$. The contribution of each spherical harmonic to the open flux on the source surface reduces as $(r_{ss}/r_\odot)^{-\ell-2}$ (Equation 10). As long as the spherical harmonics of the input B_r map do not scale exponentially with ℓ, the increasing open flux error with ℓ within pfsspy will be suppressed by the $(r_{ss}/r_\odot)^{-\ell-2}$ factor, preventing the total open flux error growing when summing over multiple harmonics.

4.3. *Field line connectivity*

From a regularly spaced grid of field line seed points on the source surface analytic solar surface field line footpoints are calculated using Equations 26 and 30 and the numerical field line footpoints computed using pfsspy . Figure 3 shows the difference between the analytic and traced solar surface footpoints in latitude (top panel) and longitude (lower panel) for $\ell, m = 3, 3$ a step size of $\Delta s = 1$, and a radial grid size of $n_r = 40$. Overall the errors are small in both latitude and longitude at $\leq 0.5°$.

There are two situations where pfsspy fails to correctly trace the field lines. The first is near polarity inversion lines, which occur at $30°, 90°, 150°, ...$ in Figure 3. Traced field lines started near polarity inversion lines on the source surface turn around and return immediately to the source surface. This is due to finite resolution effects within the model. pfsspy automatically tags these field lines as incorrectly traced, and they show up as thin white strips in Figure 3. This occurs at all spherical harmonic numbers, but only for a limited number of field lines near polarity inversion lines.

The second situation occurs near polarity inversion lines at high latitudes, when the inversion line in the model is slightly displaced from the expected inversion line. This causes field lines to deviate strongly in longitude from their analytic solution, as seen in the bottom panel of Figure 3 where a few points have large errors outside the range of the errorbars. This is due to a combination of finite resolution effects and no attempt by the tracer to handle the spherical coordinate singularity at the poles. Up to $\ell = 3$ it only occurs for $\ell = 3$ and $m = -3, 3$.

To quantify how errors in field line tracing vary with tracing step size we produce error maps like Figure 3 for a range of spherical harmonic numbers. Figure 4 shows how the maximum error in field line footpoint across a whole map varies with step size for different spherical harmonics. Errors with absolute values $> 10°$ are excluded from these plots, to exclude any points that are incorrectly traced near the polarity inversion line (see previous paragraph).

With decreasing magnetic field tracing step size, the maximum error drops off until reaching a plateau at a step size of ~ 4. Because the field line integrator uses a 4th order Runge-Kutta method, it samples the field at $1/4$ of the step size, so a levelling off of the error at a step size of around 4 is expected. Below this the integrator samples at sub-grid resolution, and the error is dominated by the error in the magnetic field solution itself. This result justifies our default choice of $\Delta s = 1$ for the other tests. Making the integration step size any smaller than $\Delta s = 1$ increases computation and memory use, but does not increase the accuracy at which the field lines are traced.

5. CONCLUSIONS

We have derived a set of analytical closed solutions for the PFSS equations when the input magnetic field is a single spherical harmonic (Section 2.1), along with analytical equations for magnetic field lines traced through these solutions (Section 2.3). These solutions have then been used to test and quantify the accuracy of the numerical pfsspy solver (Section 4).

This set of tests reveal both the accuracy and limitations of the pfsspy solver. The total open magnetic flux is systematically overestimated within the pfsspy solver, but when the number of radial grid cells exceeds 40 is accurate to within 6% of the true value for individual spherical harmonics (Figure 2). When tracing field lines from the source surface to the solar surface, pfsspy is always accurate to within $0.5°$ with a small enough tracer step size (Figure 4), but large errors in field line tracing can occur near polarity inversion lines and at the poles (Figure 3). Note that our tests use spherical harmonic solutions which are relatively smooth functions, so different tests are needed to understand how accurate the field line tracing is in areas of rapidly changing magnetic field, e.g., surrounding active regions.

These test problems form a solid benchmark for PFSS solvers and their ability to reproduce stellar potential magnetic fields accurately. We recommend that all PFSS solvers be tested against the analytical test problems presented here.
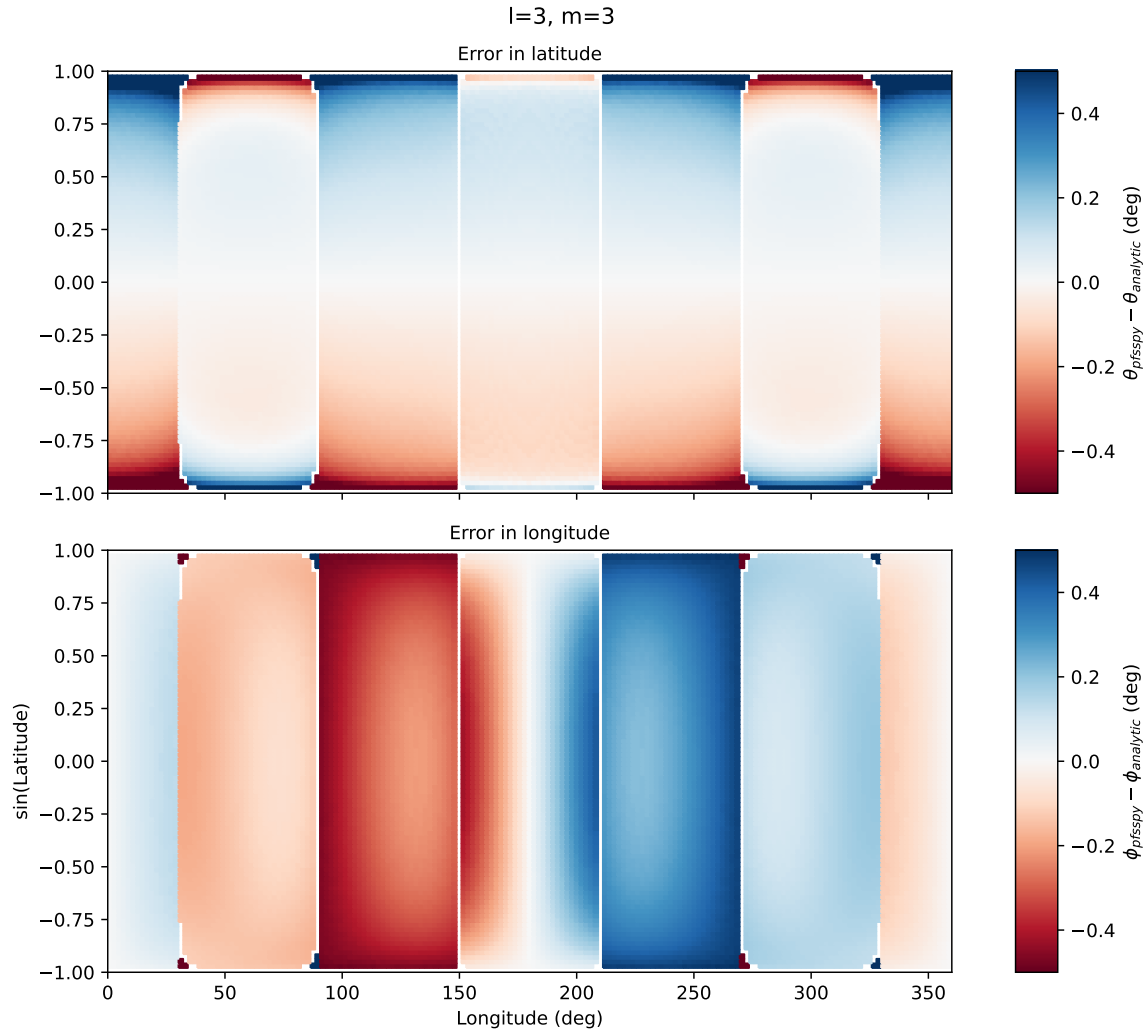
Figure 3. The difference between numerically traced and analytic solar surface footpoint latitude (top panel) and longitude (bottom panel), for $l = 3, m = 3$ and a tracer step size of $\Delta s = 1$. Field lines are traced downwards from an evenly spaced grid on the source surface.

REFERENCES

Altschuler, M. D., & Newkirk, G. 1969, Solar Physics, 9, 131, doi: 10.1007/BF00145734

Badman, S. T., Bale, S. D., Oliveros, J. C. M., et al. 2020, The Astrophysical Journal Supplement Series, 246, 23, doi: 10.3847/1538-4365/ab4da7

Baker, D., Mihailescu, T., Démoulin, P., et al. 2021, Solar Physics, 296, 103, doi: 10.1007/s11207-021-01849-7

Boe, B., Habbal, S., & Druckmüller, M. 2020, The Astrophysical Journal, 895, 123, doi: 10.3847/1538-4357/ab8ae6

Caplan, R. M., Downs, C., Linker, J. A., & Mikic, Z. 2021, The Astrophysical Journal, 915, 44, doi: 10.3847/1538-4357/abfd2f

DeRosa, M. L., Brun, A. S., & Hoeksema, J. T. 2012, The Astrophysical Journal, 757, 96, doi: 10.1088/0004-637X/757/1/96

Fargette, N., Lavraud, B., Rouillard, A. P., et al. 2021, The Astrophysical Journal, 919, 96, doi: 10.3847/1538-4357/ac1112

Gregory, S. G. 2011, American Journal of Physics, 79, 461, doi: 10.1119/1.3549206

Hakamada, K. 1995, Solar Physics, 159, 89, doi: 10.1007/BF00733033

Harris, C. R., Millman, K. J., van der Walt, S. J., et al. 2020, Nature, 585, 357, doi: 10.1038/s41586-020-2649-2
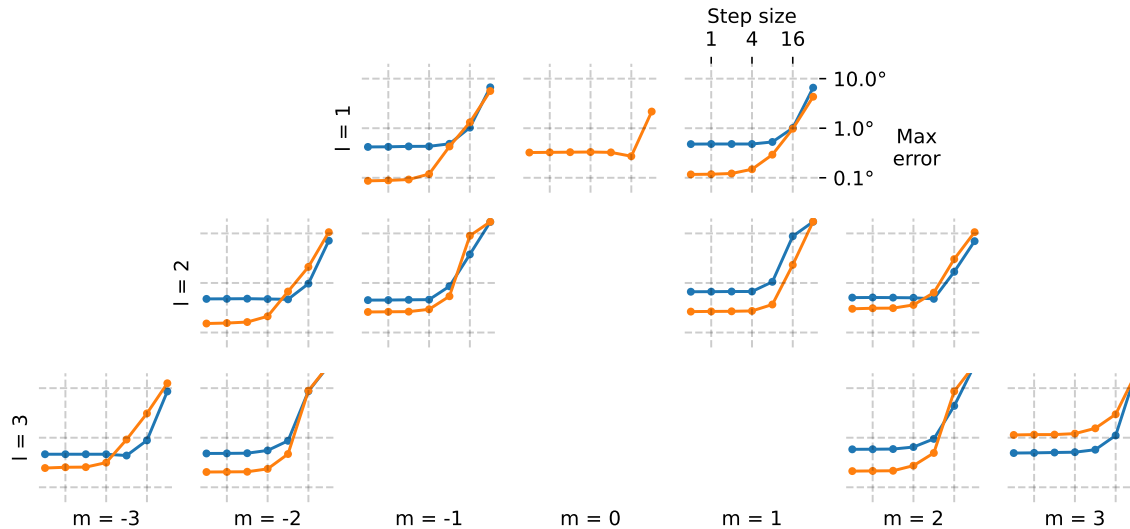
Figure 4. Maximum error in field line footpoints as a function of tracer step size for various spherical harmonics. Error in longitude is shown in blue and error in latitude in orange. Errors with absolute values $> 10°$ are excluded in these plots - this can occur close to polarity inversion lines on the source surface.

Jardine, M., Vidotto, A. A., & See, V. 2017, Monthly Notices of the Royal Astronomical Society: Letters, 465, L25, doi: 10.1093/mnrasl/slw206

Jiang, C., & Feng, X. 2012, Solar Physics, 281, 621, doi: 10.1007/s11207-012-0074-x

Kochukhov, O. 2020, The Astronomy and Astrophysics Review, 29, 1, doi: 10.1007/s00159-020-00130-3

Mackay, D. H., & Yeates, A. R. 2012, Living Reviews in Solar Physics, 9, 6, doi: 10.12942/lrsp-2012-6

Meurer, A., Smith, C. P., Paprocki, M., et al. 2017, PeerJ Computer Science, 3, e103, doi: 10.7717/peerj-cs.103

Neugebauer, M., Forsyth, R. J., Galvin, A. B., et al. 1998, Journal of Geophysical Research: Space Physics, 103, 14587, doi: 10.1029/98JA00798

Reback, J., jbrockmendel, McKinney, W., et al. 2021, Pandas-Dev/Pandas: Pandas 1.3.4, Zenodo, doi: 10.5281/zenodo.5574486

Saikia, S. B., Jin, M., Johnstone, C. P., et al. 2020, Astronomy & Astrophysics, 635, A178, doi: 10.1051/0004-6361/201937107

Schatten, K. H., Wilcox, J. M., & Ness, N. F. 1969, Solar Physics, 6, 442, doi: 10.1007/BF00146478

Sod, G. A. 1978, Journal of Computational Physics, 27, 1, doi: 10.1016/0021-9991(78)90023-2

Stansby, D., Badman, S., Ancellin, M., & Barnes, W. 2022, Dstansby/Pfsspy: Pfsspy 1.1.0, Zenodo, doi: 10.5281/zenodo.5879440

Stansby, D., Berčič, L., Matteini, L., et al. 2020a, Astronomy & Astrophysics, doi: 10.1051/0004-6361/202039789

Stansby, D., Green, L. M., van Driel-Gesztelyi, L., & Horbury, T. S. 2021, Solar Physics, 296, 116, doi: 10.1007/s11207-021-01861-x

Stansby, D., Yeates, A., & Badman, S. T. 2020b, Journal of Open Source Software, 5, 2732, doi: 10.21105/joss.02732

The Astropy Collaboration, Price-Whelan, A. M., Sipőcz, B. M., et al. 2018, The Astronomical Journal, 156, 123, doi: 10.3847/1538-3881/aabc4f

Tóth, G., van der Holst, B., & Huang, Z. 2011, The Astrophysical Journal, 732, 102, doi: 10.1088/0004-637X/732/2/102

van Ballegooijen, A. A., Priest, E. R., & Mackay, D. H. 2000, The Astrophysical Journal, 539, 983, doi: 10.1086/309265

van Driel-Gesztelyi, L., Culhane, J. L., Baker, D., et al. 2012, Solar Physics, 281, 237, doi: 10.1007/s11207-012-0076-8

Virtanen, P., Gommers, R., Oliphant, T. E., et al. 2020, Nature Methods, 17, 261, doi: 10.1038/s41592-019-0686-2

Wang, Y.-M., & Sheeley, Jr., N. R. 1992, The Astrophysical Journal, 392, 310, doi: 10.1086/171430